Atmospheric Research 249 (2021) 105307

Contents lists available at ScienceDirect

Atmospheric Research

journal homepage: www.elsevier.com/locate/atmosres

# The diurnal variability of precipitable water vapor derived from GPS tropospheric path delays over the Eastern Mediterranean

Shlomi Ziskin Ziv [a,b], Yoav Yair [c], Pinhas Alpert [d], Leenes Uzan [e,f], Yuval Reuveni [a,b,c,*]

[a] Department of Physics, Ariel University, Ariel, Israel
[b] Eastern R&D center, Ariel, Israel
[c] School of Sustainability, Interdisciplinary Center (IDC) Herzliya, Israel
[d] Department of Geophysics, Tel-Aviv University, Tel Aviv, Israel
[e] Porter School of the Environment and Earth Sciences, Raymond and Beverly Sackler Faculty of Exact Sciences, Tel-Aviv University, Tel Aviv, Israel
[f] The Israeli Meteorological Service, Bet-Dagan, Israel

ARTICLE INFO

*Keywords:*
Precipitable Water Vapor (PWV)
GPS tropospheric path delays
Mediterranean Sea Breeze (MSB)
Mixing Layer Height (MLH)
Diurnal variations

ABSTRACT

The study of the diurnal variations of the total water vapor amount in an atmospheric column, also known as Precipitable Water Vapor (PWV) or Integrated Water Vapor (IWV), is highly significant in meteorology and climatology studies, yet very limited due to insufficient spatial and temporal in situ measurements. Nowadays, Global Navigation Satellite System (GNSS) ground receivers are used along with retrieval techniques in order to conduct high sample rate PWV estimations. Here, we present the annual and seasonal PWV diurnal cycles extracted from the Survey Of Israel Active Permanent Network (SOI-APN) GNSS receivers in the Eastern Mediterranean region. The data period spans from 5 to 21 years, ensuring its suitability for studying the PWV annual and seasonal mean diurnal variations. We particularly focus on the summer months (JJA), where the Mediterranean Sea Breeze (MSB) plays a dominant role in transporting humidity inland. For most stations, the diurnal amplitude in summer is the highest compared to the seasonal mean (4%–21%), followed by spring, autumn and winter (2%–4%). The PWV in the coastal stations peaks at 6–7 UTC while the northernmost highland station peaks at 8 UTC and the southernmost at 14 UTC indicating frontal MSB propagation from the coastline eastward inland combined with northern winds enhancement due to Coriolis force. Moreover, for most stations, the PWV peak hour is correlated with the distance from the Mediterranean Sea shore, substantiating the MSB's role as a key driver of the PWV diurnal variability during summer months. The PWV minimum values in the coastal stations occurs between 14 UTC and 19 UTC while in the highland stations it varies from 17 to 00 UTC. The coastal stations' PWV amplitude, compared to the daily mean, is around 1 mm while the highland stations amplitude is 2–3 mm. In addition, a strong correlation between the PWV diurnal cycle and the atmospheric Mixing Layer Height (MLH) diurnal variations is found using ceilometer data, suggesting that the MLH modulates the PWV, however this conclusion requires further research. Finally, using harmonic analysis with the PWV diurnal variations in summer, reveals that the diurnal and the semidiurnal modes account for ~95% of the sub-daily variance in 19 out of 21 GNSS stations

## 1. Introduction

Water vapor (WV) is an important and most abundant greenhouse gas in the thermodynamic engine of the troposphere. It is a key component in various phenomena ranging from precipitation, cloud formation to tropical cyclones and severe thunderstorms. Thus, it is important to understand the factors that control the variability of atmospheric WV (Soden et al., 2004). Currently, our ability to constantly monitor changes in atmospheric WV at a high spatial resolution, particularly above the surface, is insufficient since water vapor varies considerably in space and time (Trenberth et al., 2005; Chen and Liu, 2016).

There are several methods for estimating the WV amount in the atmosphere. These include direct humidity measurements via a launched radiosonde (Elliott et al., 1991; Miloshevich et al., 2006) or retrieved WV profiles from ground-based platforms such as microwave

* Corresponding author at: Department of Physics, Faculty of Natural Sciences, Ariel University, Science Park, Ariel 40700, Israel.
*E-mail address:* yuvalr@ariel.ac.il (Y. Reuveni).

https://doi.org/10.1016/j.atmosres.2020.105307
Received 29 July 2020; Received in revised form 30 September 2020; Accepted 11 October 2020
Available online 17 October 2020

radiometers and sun photometers (Westwater, 1978; Ichoku et al., 2002; Pérez-Ramírez et al., 2014). Other techniques involve remote sensing satellites observing the emitted infrared (IR) radiation in the WV absorption bands (Van de Berg et al., 1995; Velden et al., 1997; Leontiev and Reuveni, 2017, 2018). The approach we use in this work is to estimate the Precipitable Water Vapor (PWV) amount from the tropospheric path delay time of the signal that is transmitted via the Global Positioning System (GPS) satellites to ground-based receivers (Bevis et al., 1992, 1994).

### 1.1. Global Navigation Satellite System (GNSS) meteorology

Radio signals that are transmitted from a GPS satellite orbiting at an altitude of ≈20,200 km are first dispersed in the ionosphere and then absorbed in the troposphere resulting in a measurable time delay in the ground-based receiver. Since GPS satellites transmit signals at least in two frequency bands (e.g., L1 = 1575.42 MHz, L2 = 1227.6 MHz and L5 = 1176.45 MHz), the path delay from the ionospheric dispersion can be accounted for by using ionosphere-free combination and/or models (Eueler and Goad, 1991; Reuveni et al., 2015). The remaining delay, that is due to tropospheric absorption, is referred as Zenith Total Delay (ZTD)[1] and is divided into two components, both explained by two different absorption processes in the troposphere. The Zenith Hydrostatic Delay (ZHD) is associated with the induced dipole moment of all the atmospheric gases except water vapor, and is mainly a function of the atmospheric pressure (Davis et al., 1985). The Zenith Wet Delay (ZWD) which is associated with the permanent dipole moment of the water molecule (Thayer, 1974), can be estimated by subtracting the ZHD from the ZTD.

The received radio signals from the satellite are saved in text files called RINEX (Receiver Independent Exchange Format) and can be processed by specialized software such as NASA's JPL GipsyX (Bar-Sever, 2016). This processing involves complex inversion algorithms (Webb and Zumberge, 1993; Duan et al., 1996) for retrieving the ZTD and modelling the ZHD using global empirical mapping functions (Böhm et al., 2006b; Reuveni et al., 2012, 2014). Since ZWD is proportional to the total amount of water vapor present in a vertical atmospheric column, we can translate ZWD into PWV[2] using a water vapor weighted mean temperature (Davis et al., 1985).

The quality of GNSS derived PWV has been demonstrated through comparison to radiosonde measurements, radiometers, sun photometers and reanalysis products with RMSE ranging from 1 to 3 mm (Li et al., 2003; Van Baelen et al., 2005; Wang et al., 2007; Pérez-Ramírez et al., 2014; Wang et al., 2017). Furthermore, the high temporal resolution (e.g., 5 min) of the GNSS derived PWV is suitable for studying the diurnal variations of WV distribution in the atmosphere (Dai et al., 2002; Ortiz de Galisteo et al., 2011; Kalinnikov and Khutorova, 2017).

### 1.2. Humidity in the Eastern Mediterranean

The main source of humidity in the study area is the Mediterranean Sea where the primary transport mechanism on a diurnal time scale is the Mediterranean See Breeze (MSB).[3] During daytime, a sea breeze is created in response to the land-sea differential heating. The resulting horizontal pressure gradient drives the cool and humid marine air towards inland. After sunset, the land cools faster than the sea thus reversing the pressure gradient force and driving dry air from inland towards the sea (i.e., land breeze). Thorough reviews about the land-sea breeze mechanism are available in the literature (e.g., Simpson (1994); Crosman and Horel (2010)).

In the summer season (JJA), the MSB is superimposed on the prevailing cool and moist Etesian winds that are associated with the large-scale synoptic forcing of the Persian Trough (PT) (Ziv et al., 2004). Moreover, in summer, the entire Eastern Mediterranean region is subjected to a semi-permanent subsidence (Rodwell and Hoskins, 1996) which is coupled with the PT and enhances the inversion layer in the Planetary Boundary Layer (PBL) (Dayan et al., 2002; Ziv and Saaroni, 2011), thus effectively lowering the Mixing Layer Height (MLH).

Both the coastal and marine mixing layer heights are important factors which allow the MSB to effectively advect humidity. Indeed, Shilo et al. (2015) concluded that synoptic situations leading to Etesian winds weakening or imposing a reduction in the average height of the marine layer, can weaken or even block the MSB from penetrating inland. Moreover, even for stable summer conditions when the Persian Trough is weak or non-existent, the coastal mixing layer height increases as the sea breeze front penetrates inland (Uzan et al., 2016, 2019).

The goal of the present study is to characterize the PWV diurnal cycle climatology across 21 Survey Of Israel GNSS stations in the Eastern Mediterranean while focusing on the summer season.

## 2. Data and methodology

The Survey Of Israel Active Permanent Network (SOI-APN) is comprised of 22 GNSS ground stations where only 21 of them were found suitable for our study. Their names are specified in Table 1 and their locations are designated on the map in Fig. 1, along with the locations of the Israeli Meteorological Service (IMS) automated stations. The stations' locations are conveniently correlated with the region's climate zones effectively representing the coastal area, central ridge inland area and the Negev desert.

The ZWD time series are produced by processing the raw RINEX files and are subsequently transformed into PWV time series. We elaborate upon the ZWD processing and the GNSS station selection procedure in Section 2.1. The conversion of ZWD to PWV and the production of annual and seasonal diurnal means is outlined in Section 2.2. The diurnal means for JJA months are then subjected to harmonic analysis as described in Section 2.3.

Furthermore, in the spirit of reproducible science, we encourage the interested reader to explore the Python repository hosted on GitHub.com (https://github.com/ZiskinZiv/PW_from_GPS) that includes the procedures used in this analysis. The PWV data in all of the processing stages will be available via ftp server by a specific email request.

### 2.1. Zenith wet delay processing

The daily RINEX files from the SOI-APN are periodically uploaded to the SOPAC/Garner GPS archive (http://garner.ucsd.edu/). Fig. 1 shows the data availability of the SOI-APN and the stations' position on the map. Clearly, there are some gaps in the data availability as well as partial data due to station termination. Although these gaps can be filled by climatology or even interpolation, it is not the philosophy of this work.

Subsequently, we process the daily RINEX files with NASA's JPL GipsyX (Bar-Sever, 2016) software. The processing involves Precise Point Positioning (PPP) which provides us with the station's precise latitude, longitude and altitude (above sea level). We use most of the default parameters for the PPP, which include a minimum cutoff elevation angle of 7°, Global Mapping Function (GMF) for the tropospheric model (Böhm et al., 2006a) and ocean loading for all of the stations. The full parameter tree used in this work is available at the Github.com repository (https://github.com/ZiskinZiv/PW_from_GPS/blob/master/my_trees/ISROcnld/ISROcnld_0.tree). GipsyX employs optimization techniques in order to provide better accuracy for the final ZWD solution. Thus, with the default parameters, each RINEX file with a 30 s sample rate is processed and down-sampled to a 5 min ZWD

[1] Sometimes referred to as Zenith Tropospheric Delay.

[2] Synonymous with PW, TPW and IWV (although with different units - see Section 2.2).

[3] Except for areas close to the Sea of Galilee and the Red Sea where the MSB interacts with the local moisture field.

**Table 1**
Geographical coordinates, altitude above sea level, distance from the Mediterranean sea shore and location of the GNSS network analysed in this work.

| GNSS station name | Station ID | Latitude [°N] | Longitude [°E] | Altitude [m a.s.l] | Distance from shore [km] | Location |
|---|---|---|---|---|---|---|
| Kibutz Kabri | KABR | 33.02 | 35.15 | 103 | 5 | Coastal |
| Binyamin Shmuter Memorial site | BSHM | 32.78 | 35.02 | 225 | 5 | Coastal |
| Ceasarya | CSAR | 32.49 | 34.89 | 36 | 0 | Coastal |
| Tel Aviv | TELA | 32.07 | 34.78 | 58 | 2 | Coastal |
| Waste treatment facility, Ashkelon | ALON | 31.71 | 34.61 | 55 | 3 | Coastal |
| Kibutz Cerem Shalom | SLOM[a] | 31.23 | 34.28 | 112 | 12 | Coastal |
| Nizana | NIZN[a] | 30.88 | 34.42 | 274 | 51 | Coastal |
| Beit Rimon | NZRT | 32.78 | 35.33 | 411 | 26 | Highland |
| Kibbutz Merav | MRAV | 32.45 | 35.42 | 415 | 49 | Highland |
| Ariel | YOSH | 32.10 | 35.21 | 714 | 39 | Highland |
| Jerusalem | JSLM | 31.77 | 35.20 | 790 | 50 | Highland |
| Kibutz Lahav | KLHV | 31.38 | 34.87 | 498 | 43 | Highland |
| Yerucham | YRCM | 30.99 | 34.93 | 516 | 74 | Highland |
| Mitzpe Ramon | RAMO | 30.60 | 34.76 | 886 | 95 | Highland |
| Kibutz el-rom | ELRO | 33.18 | 35.77 | 1083 | 52 | Eastern |
| Katzrin | KATZ | 33.00 | 35.69 | 346 | 51 | Eastern |
| Metzoki dragot | DRAG | 31.59 | 35.39 | 31 | 75 | Eastern |
| Ded-Sea Manufactories | DSEA | 31.04 | 35.37 | −360 | 103 | Eastern |
| Sapir | SPIR | 30.61 | 35.18 | 12 | 120 | Eastern |
| Kibutz Neve Harif | NRIF | 30.04 | 35.04 | 457 | 162 | Eastern |
| Eilat | ELAT | 29.51 | 34.92 | 29 | 208 | Eastern |

[a] Station is located inland, see Fig. 1 for more accurate location.

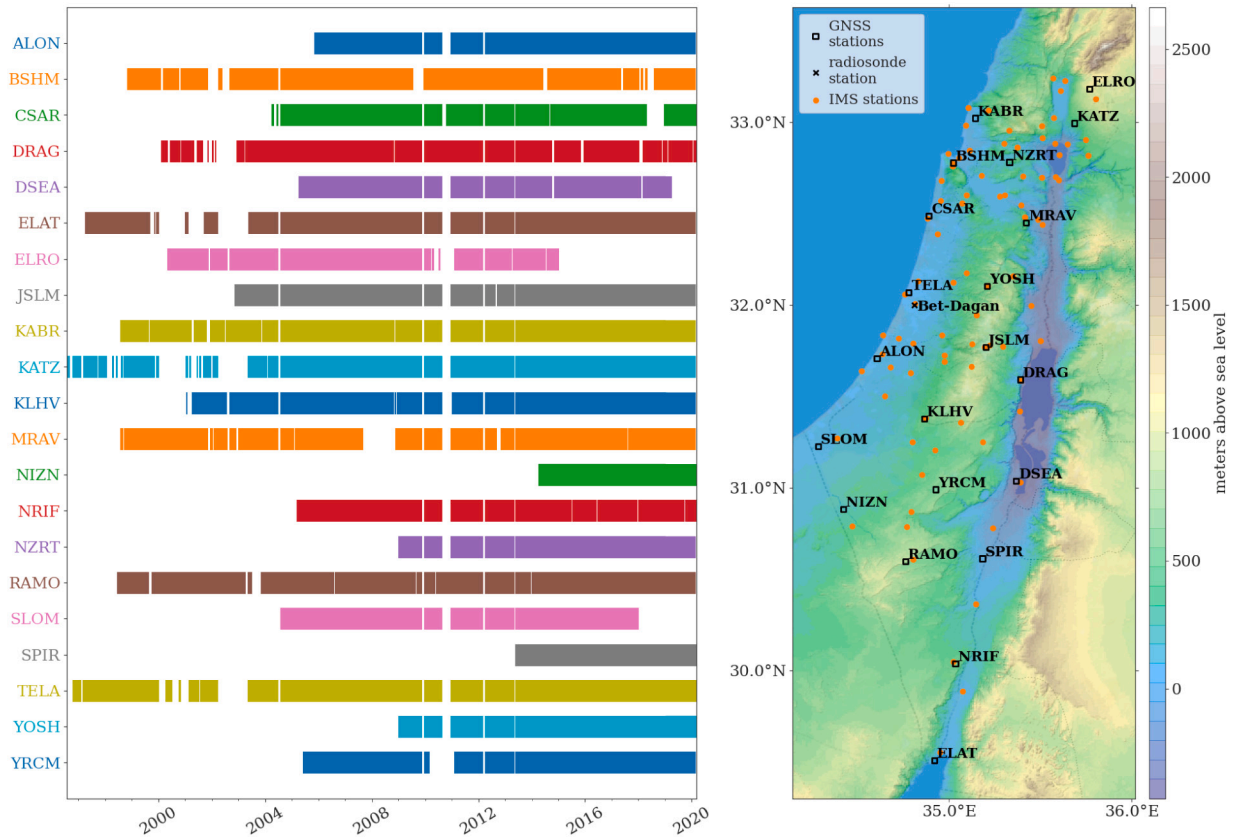


**Fig. 1.** Left: PWV data availability for each of the Survey Of Israel Active Permanent Network (SOI-APN) shown in various colors for distinction. Right: The SOI-APN receivers (black squares), ~88 Israeli Meteorological Service (IMS) stations (filled orange circles) and Bet-Dagan radiosonde station (black x) plotted on a height filled contour map of the study area. (For interpretation of the references to colour in this figure legend, the reader is referred to the web version of this article.)

solution. An example of a processed daily ZWD solution of TELA station can be seen in Fig. 2.

Since GipsyX employs a stochastic filtering method for the retrieval of the daily ZWD, there is a small difference between the end of one daily ZWD solution to the start of the next daily ZWD solution. We resolve this small discontinuity by merging three consecutive daily RINEX files into one 30 h RINEX file (centered on 12:00 PM from the middle daily RINEX file). The overlapping segments of each consecutive 30 h solution are averaged and smoothed to obtain a continuous long-term ZWD time series (e.g., Figs. 2, 3). For the completion of the long-term ZWD time series, we repeat the overlapping segments smoothing procedure for all the daily ZWD solutions. Finally, we filter the outliers of the ZWD time series by removing data points that are at least twice the Inter-Quartile Range (IQR with k = 2). The IQR is defined as the difference between the

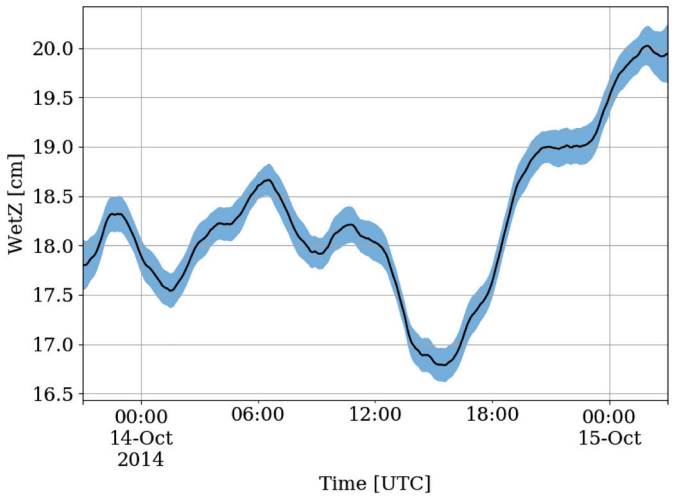


**Fig. 2.** Zenith Wet Delay from GNSS station TELA in 2014-10-14. Note the error estimation from the GipsyX software (filled).

$75^{th}$ and $25^{th}$ percentiles.

The obtained long-term ZWD time series are then subjected to a simple selection criteria. We drop incomplete days if they are missing half or more data points and repeat the same criteria for incomplete months. The missing days and months that were dropped from the all the stations consist of about 1% and 3% respectively. Furthermore, we drop HRMN station for having non-physical values (i.e., ZWD $< 0$) due to snow build-up on the antenna during winter.

Originally, our station database included LHAV station and GILB station. On December 2008, LHAV station was moved ~40 m inside Kibutz Lahav and was renamed to KLHV. The GILB station was moved ~3.3 km to the neighbouring Kibutz Merav on September 2012 and was therefore renamed to MRAV. Thus, we decided to merge them and keep their new names, with the assumption that each set of merged stations should represent the same geographical region. The merging is done by accounting for the ZWD mean difference due to station elevation. To this end, we estimate the empirical ZWD "lapse rate" using the ZWD means of all the stations in our network, with the assumption that the drop in ZWD with height is approximately linear for low altitudes. Fig. 4 shows the ZWD mean of each station's time series vs. its altitude above sea level. The linear trend is calculated using a simple linear regression and produces a slope of 4.48 cm/km. Thus, a station within our network, located at 1 km above sea level has a mean ZWD of 4.48 cm less than a station located at sea level.

### 2.2. PWV diurnal cycle production

PWV is defined as the height of an equivalent column of liquid water and can be translated from ZWD using the following formula (Bevis et al., 1994):

$$\mathrm{PWV} = \Pi \times \mathrm{ZWD} \tag{1}$$

$\Pi$ is the dimensionless constant of proportionality and is defined as:

$$\Pi = \frac{10^6}{\rho_w R_v \left(k_2' + \frac{k_3}{T_m}\right)} \tag{2}$$

where $\rho_w$ is the liquid water density, $R_v = 461.52$ J (kg K)$^{-1}$ is the specific gas constant for water vapor and $k_3 = (3.776 \pm 0.004) \times 10^5$ K$^2$ mb$^{-1}$ and $k_2' = 22.1 \pm 2.2$ K mb$^{-1}$ are empirical parameters that were used in Bevis et al. (1992) and Bevis et al. (1994) respectively. In the literature, PWV is sometimes referred to as Integrated Water Vapor (IWV) which has units of kg m$^{-2}$. From Eq. (1) we see that the IWV is simply $\rho_w \Pi \times$ ZWD and is numerically equivalent to PWV although with

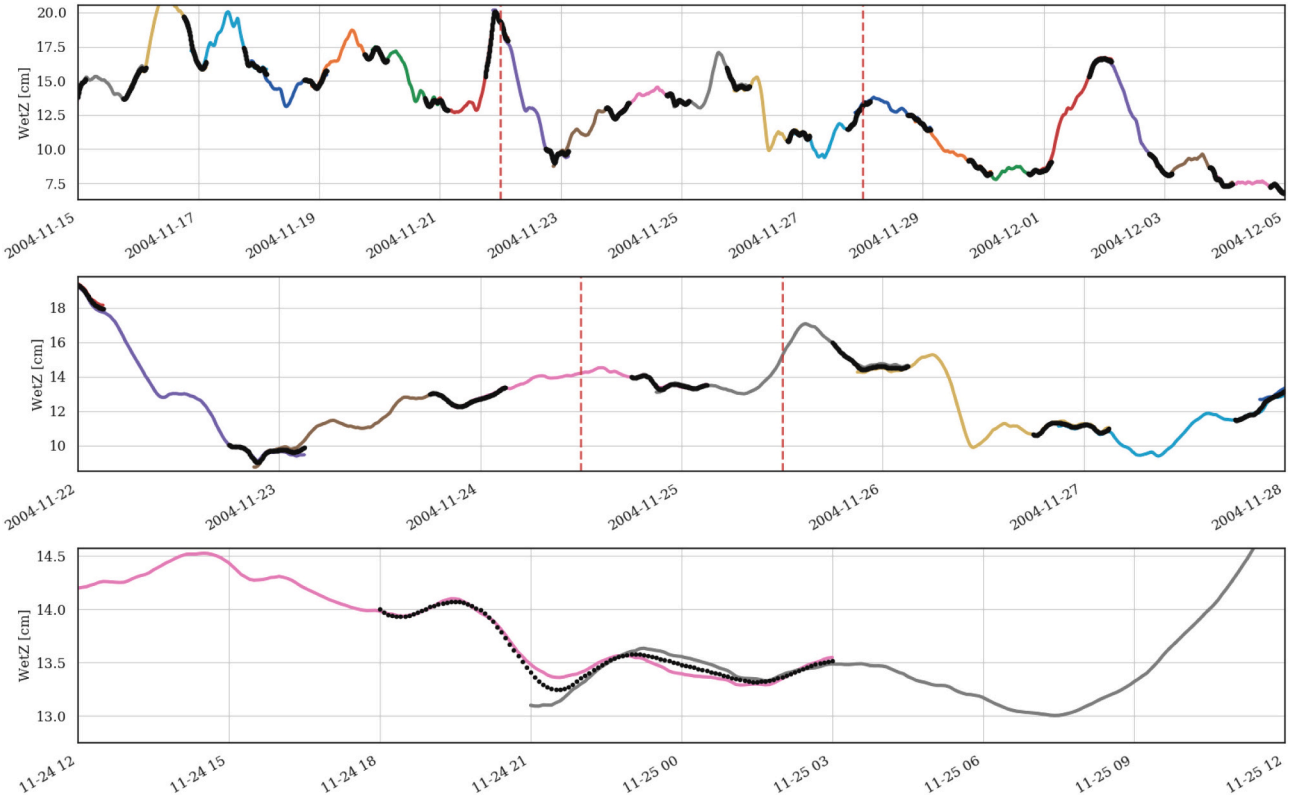


**Fig. 3.** 20, 6 and 1 days of zenith wet delay in 2004 from the TELA GNSS station for the top, middle and bottom figures respectively. The colored segments represent daily solutions while the black dots represent smoothed mean solutions.

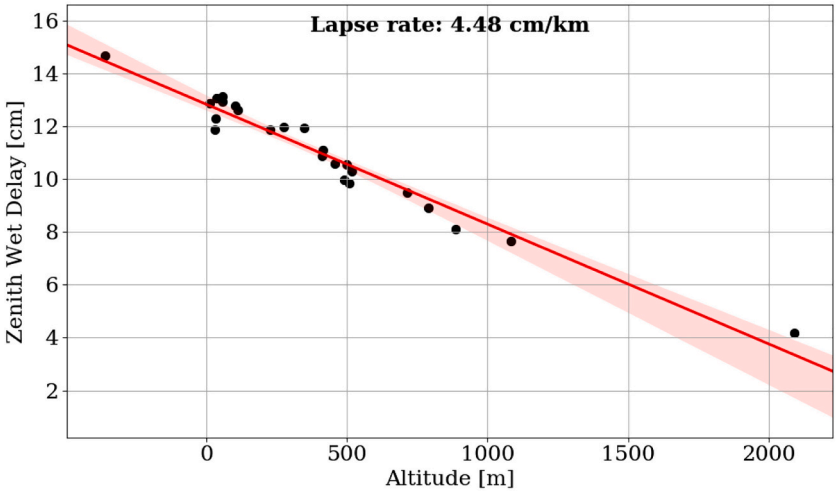


**Fig. 4.** The ZWD mean for each station in the SOI-APN vs. its altitude above sea level.

different units. Thus, 1 kg $m^{-2}$ of IWV is equivalent to 1 mm of PWV.

$T_m$ is the water vapor weighted mean atmospheric temperature as defined in Davis et al. (1985):

$$T_m = \frac{\int (P_v/T)dz}{\int (P_v/T^2)dz} \tag{3}$$

where $P_v$ and $T$ are the water vapor partial pressure and air temperature respectively and both are functions of $z$ (height above sea level). From Eq. (2), if we assume that $T_m \sim 10^2$ K, we see that $\Pi$ is a linear function of $T_m$ ($k_2' << \frac{k_3}{T_m}$), and for a typical $T_m$ (288 K) we get a $\Pi$ value of 1.625. Since ZWD is conveniently given in centimeters, 1 cm of ZWD translates to a 1.625 mm of PWV.

In order to calculate $T_m$ over each GNSS station, we need the surface temperature measurements, $T_s$ at each GNSS station, and a method to estimate $T_m$ from $T_s$ measurements. The method described in Bevis et al. (1992) used radiosonde profiles in order to find the relationship between the surface temperature ($T_s$) and $T_m$ in Northern America ($T_m = 0.72T_s + 70.2$) using a linear fit. Thus, we use the same procedure in order to find this relationship in our study area:

$$T_m = 0.69T_s + 82 \tag{4}$$

Eq. (4) is found using the data of the IMS Bet-Dagan radiosonde station (location is in Fig. 1). For each upper air sounding profile, we calculate $T_m$ using Eq. (3) and plot it against the surface temperature $T_s$. As can be seen from Fig. 5, we used 8370 upper air profiles (spanning 11.5 years) and obtained an RMSE of 4 K.

One notable attempt in trying to lower the RMSE by using different time selection criteria such as hour of the day (00:00 and 12:00) and seasons of the year (e.g., winter), yielded a good exercise in residual statistics but ultimately resulted in negligible effect.

The IMS also maintains and operates ~88 automated stations (see Fig. 1) that measure temperature at 10 min interval. However, some stations have gaps in their time series and their location is near but not exact as the GNSS stations. Thus, we fill the surface temperature gaps with mean Day Of Year climatology and mean diurnal climatology for each station and we use Ordinary Kriging (OK, https://github.com/GeoStat-Framework/PyKrigePyKrige), (Cressie, 1988) spatial interpolation scheme in order to receive the surface temperature at the GNSS stations' locations.

Since many IMS stations have different heights, we need to account for this height difference for a successful interpolation. Thus, we estimate the empirical lapse rate using a simple linear regression and we constrain it to be between 5 and 10 °C/km. (e.g., see Fig. 6). We then use the lapse rate to set each station's temperature as if it would be in height

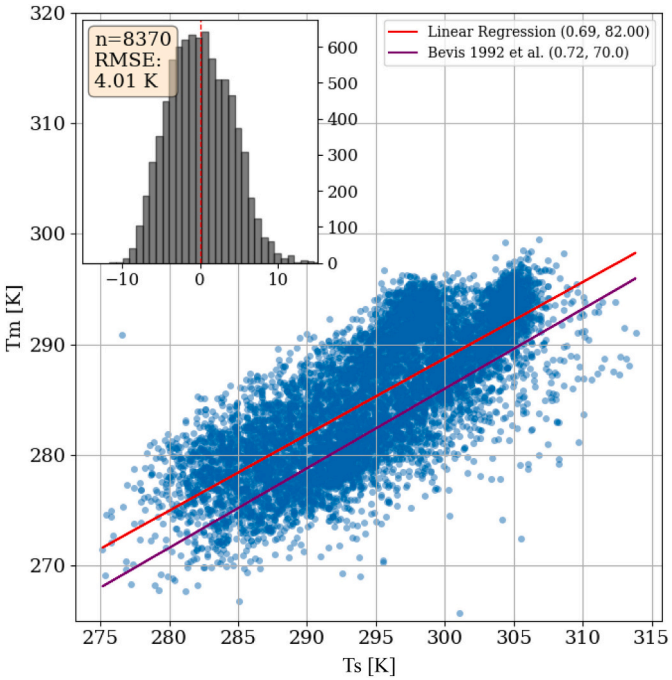


**Fig. 5.** A scatter plot of water vapor weighted mean temperature (Tm) vs. surface temperature (Ts) of the Bet-Dagan radiosonde station. Ordinary least squares linear fit (red) yields the residual distribution with RMSE of 4 K. Bevis et al. (1992) model is plotted (purple) for comparison. (For interpretation of the references to colour in this figure legend, the reader is referred to the web version of this article.)

0 above sea level, we interpolate and fix the temperature again to the station's original height.

Lastly, since our temperature data is sampled at 10 min, we upsample it to 5 min using a simple forward fill rule and translate $T_s$ into $T_m$ using Eq. (3), calculate $\Pi$ using Eq. (2) and produce the PWV time series using Eq. (1).

Upon producing the PWV time series, we choose TELA station, the closest GNSS station to Bet-Dagan radiosonde station (see the map at Fig. 1) and validate its PWV records twice daily for the years 2014–2019. The comparison with radiosonde records yielded a bias of 1.37 mm and an RMSE of 2.71 mm and is further discussed in the appendix (A).

The PWV annual mean diurnal cycle, for each station is produced as

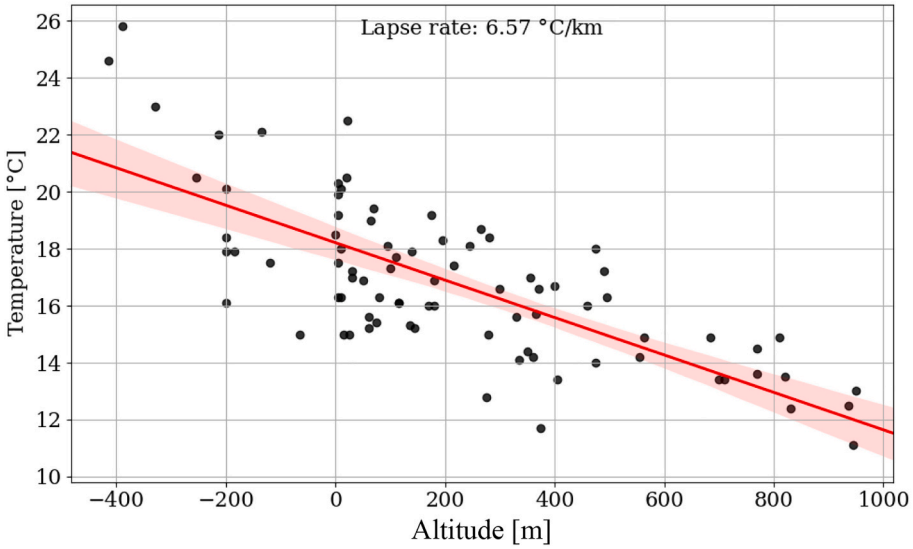


**Fig. 6.** Temperature vs. altitude for 10 PM in 2013-10-19 for all automated 10 min IMS stations. The lapse rate is calculated using ordinary least squares linear fit and is between 5 and 10 °C/km.

follows. First, we calculate the daily mean of all the data points (288 pts. per day) and subtract the daily means from the time series to produce the daily anomalies. Subsequently, we select all the daily anomalies that reside between each hour of the day (for the entire time series period, i.e., ranging from 5 to 21 years of station data) and average them. Similarly, the seasonal diurnal cycle is obtained by selecting the data points within each season separately, removing their daily means and averaging for each hour of the day. The seasons are defined as JJA (June to August), DJF (December to February), MAM (March to May) and SON (September to November).

### 2.3. Diurnal cycle harmonic analysis

Following Dai et al. (2002); Ortiz de Galisteo et al. (2011); Kalinnikov and Khutorova (2017), for each station, we used the least squares fit for the daily anomalies time series in order to find the first two harmonics using the following equation:

$$S_n(t) = A_n \cdot sin\left[2\pi f_n\left(t - t_{p,n}\right)\right] + \varepsilon_n \quad (5)$$

where n = 1, 2 for the diurnal and semidiurnal modes (S1 and S2 respectively). $f_1 = 1, f_2 = 2$ are the frequencies in cycles per day and $t_{p,n}$ is the phase term that is reported as the hour (UTC) of the reached peak. For S2, we report the phase term as the hour of the first maximum reached. $\varepsilon$ is the residual for each mode.

## 3. Results

This section includes a description of the annual and seasonal PWV diurnal cycles and is followed by a description of the diurnal harmonic analysis in summer (JJA). While the time is reported in UTC throughout this section, it is worth noting that the local solar time in the study area is UTC + 2 (in summer it is UTC + 3 due to daylight saving).

### 3.1. Diurnal cycle

Fig. 7 shows the PWV annual and the seasonal diurnal cycles for 21 SOI-APN stations in the Eastern Mediterranean. The figure is arranged as to best match the stations' locations on the map. Thus, each column has stations arranged from North to South while each row has stations arranged from West to East. The left column has all the coastal stations except for the last two (SLOM and NIZN stations) which are located inland. The middle column has all the stations that reside in the central highland region while the right column includes the most diverse stations' locations, ranging from ELRO and KATZ stations in the Golan Heights, DSEA station in the Dead sea to ELAT station near the Red sea. Most of the coastal stations have low elevation (≤100 m) except BSHM station (225 m) while the highland stations have medium elevation (400 to 900 m). The diverse group of stations to the East have various elevations ranging from −361 m in the Dead Sea (DSEA) to 1083 m at Elrom (ELRO) located on the Golan highland.

For each station, the lowest amplitude occurs in winter (DJF) and is around 0.5 mm, while the highest amplitude is in summer (JJA) with values ranging from 1 mm in the coastal stations and 2–3 mm in the highland stations. These amplitudes are consistent with previous studies in other regions (Dai et al., 2002; Ortiz de Galisteo et al., 2011; Ryu et al., 2015). The coastal stations peak at around 6–7 UTC in JJA, 7–8 UTC in MAM & SON and 8–9 UTC for DJF while the minimum value is reached between 14 and 18 UTC. For the highland stations in summer, the peak is reached at a propagating rate starting from 8 UTC at the northernmost highland station (NZRT station) and ending at 14 UTC for the southernmost highland station (RAMO station). During spring (MAM) and autumn (SON), the peak is shifted 1–2 h forward from the peak reached in summer, while for winter, for some stations, the peak is reached at 6 UTC. The minimum follows the same propagation and ranges from 18 to 0 UTC. Further east, during summer, stations ELRO and KATZ reach peak values around 10 UTC with the same 1–2 h seasonal shift as the highland stations, and the minimum is reached at 2 UTC for ELRO station and 18 UTC for KATZ station. At the Dragot station (DRAG) in summer months the amplitude is ~3–6 times higher than its other seasonal amplitudes peaking at 12 UTC and the minimum is reached at 21 UTC. Stations SPIR, NRIF and ELAT show the same peak propagation as the highland stations ranging from 16 to 21 UTC in summer with the minimum reached varies between 10 and 13 UTC. Lastly, DSEA, in summer, peaks at 5 UTC and the minimum is reached at 11 UTC.

Table 2 shows the ratios of the maximal amplitude of the annual or seasonal diurnal cycles to the annual or seasonal means for each station respectively. The annual means for each station were calculated by averaging all the data points while the seasonal means were obtained by averaging the data points within each season. This ratio can measure the relative strength of the diurnal cycle for a specific season or for the entire year. For the coastal stations, the annual ratio is around 3.5% where in JJA it is around 5% and in DJF it is around 2%. For the highland stations,

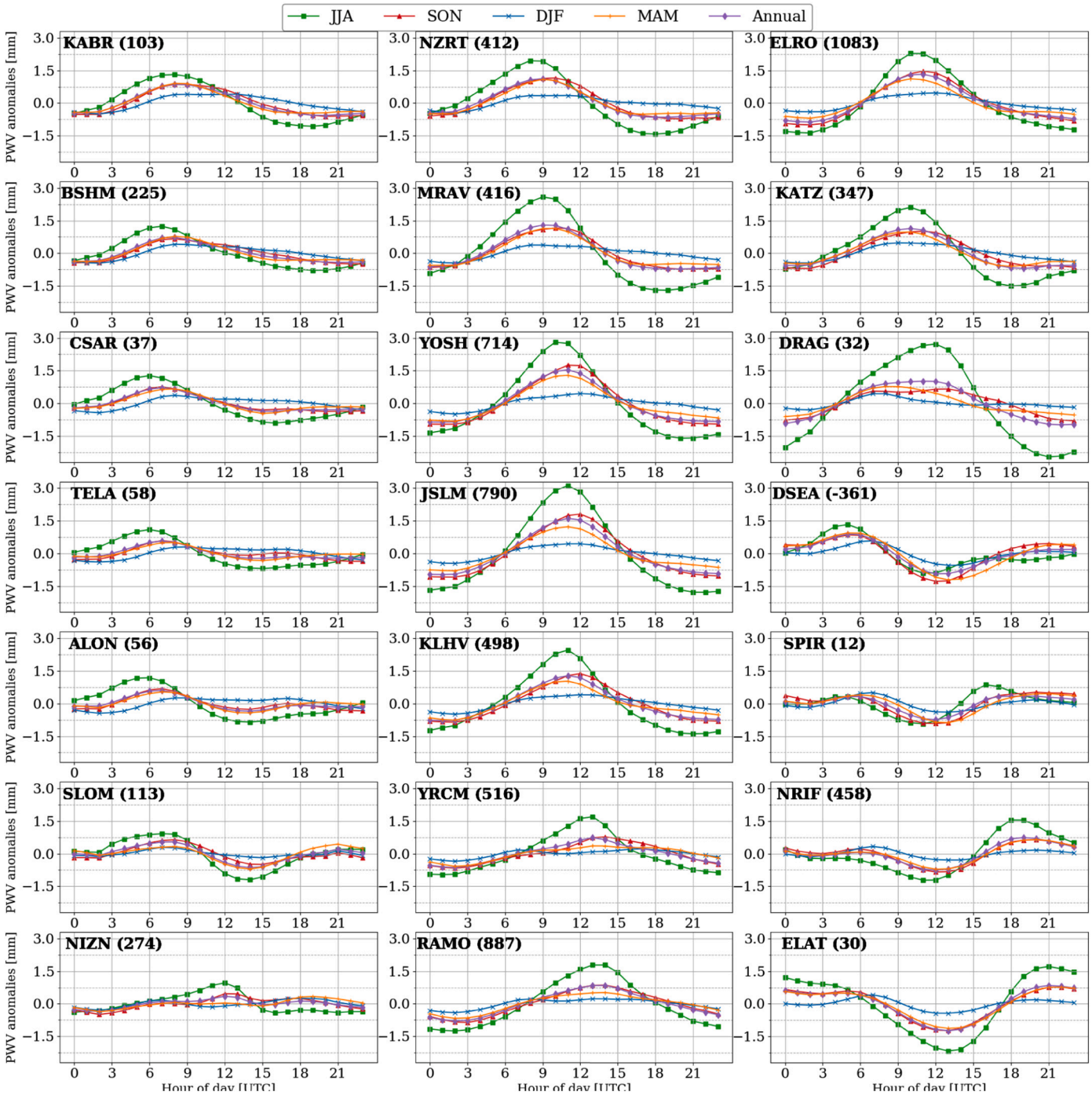


**Fig. 7.** The PWV annual and seasonal diurnal cycles of the SOI-APN stations. The panels are ordered as to best match the stations' locations on the map, so that left panels are close to the Mediterranean coast, mid-panels further inland and right panels deeper inland (Fig. 1). Green squares, red triangles, blue x's and orange +'s represent JJA, SON, DJF and MAM months respectively. Purple diamonds indicate the annual cycle. Each station ID is specified in the upper left corner of each panel followed by its height above sea level (meters) in parenthesis. (For interpretation of the references to colour in this figure legend, the reader is referred to the web version of this article.)

**Table 2**
The ratio of the PWV maximal diurnal amplitude and the annual/seasonal mean.

| Station | Location | Annual [%] | JJA [%] | SON [%] | DJF [%] | MAM [%] |
|---|---|---|---|---|---|---|
| KABR | Coastal | 4.2 | 5.7 | 3.7 | 2.8 | 5.0 |
| BSHM | Coastal | 3.8 | 6.1 | 3.0 | 2.7 | 4.5 |
| CSAR | Coastal | 3.4 | 5.4 | 3.1 | 2.4 | 3.6 |
| TELA | Coastal | 2.7 | 4.9 | 2.4 | 2.2 | 2.7 |
| ALON | Coastal | 2.9 | 5.2 | 2.7 | 2.5 | 2.9 |
| SLOM[a] | Coastal | 3.2 | 5.5 | 2.6 | 1.7 | 3.9 |
| NIZN[a] | Coastal | 1.9 | 4.6 | 2.2 | 1.8 | 2.2 |
| Mean value | Coastal | 3.2 | 5.3 | 2.8 | 2.3 | 3.5 |
| NZRT | Highland | 6.4 | 10.5 | 5.7 | 3.0 | 6.9 |
| MRAV | Highland | 7.7 | 14.8 | 5.8 | 3.0 | 7.3 |
| YOSH | Highland | 10.1 | 17.9 | 9.7 | 3.7 | 9.2 |
| JSLM | Highland | 11.4 | 21.8 | 10.6 | 3.6 | 9.4 |
| KLHV | Highland | 7.8 | 14.4 | 7.0 | 3.4 | 6.9 |
| YRCM | Highland | 4.4 | 9.8 | 3.9 | 2.5 | 3.9 |
| RAMO | Highland | 6.6 | 13.6 | 5.5 | 3.8 | 5.7 |
| Mean value | Highland | 7.8 | 14.7 | 6.9 | 3.3 | 7.0 |
| ELRO | Eastern | 10.9 | 19.6 | 10.1 | 4.3 | 9.7 |
| KATZ | Eastern | 5.9 | 10.3 | 4.6 | 2.8 | 5.7 |
| DRAG | Eastern | 5.1 | 13.2 | 3.4 | 2.5 | 4.4 |
| DSEA | Eastern | 4.0 | 5.2 | 4.6 | 2.9 | 5.9 |
| SPIR | Eastern | 3.5 | 4.1 | 3.7 | 2.9 | 4.8 |
| NRIF | Eastern | 4.5 | 8.3 | 4.1 | 2.4 | 4.7 |
| ELAT | Eastern | 6.4 | 10.4 | 5.4 | 2.7 | 6.7 |
| Mean value | Eastern | 5.8 | 10.2 | 5.1 | 2.9 | 6.0 |

[a] Station is located inland, see Fig. 1 for more accurate location.

the annual ratio ranges from 4.4% to 11.4% where again in JJA it is the highest with values ranging from 10 to 21% while in DJF all the values are around 3%. For the Eastern stations, the annual values vary between 3.5% to 11% where the summer months (JJA) have the highest values (4–20%) and the winter months (DJF) the lowest (around 3%).

### 3.2. Diurnal harmonic analysis

The harmonic analysis was employed on the PWV diurnal cycle in JJA since the summer in the Eastern Mediterranean has a semi-permanent synoptic situation that other seasons lack, as they experience transient weather systems which have different flow characteristics.

Table 3 describes the amplitude in mm, peak hour in UTC and variance explained by the diurnal and semi-diurnal cycles in summer (S1 and S2 defined above). Furthermore, Fig. 8 shows S1 and S2, their sum and the mean diurnal cycle in JJA. The total variance explained by S1 and S2 is greater than 95% for all the stations except SPIR (73.5%) and NIZN (13.3%). We should emphasize that NIZN is the only station that we were unable to reconstruct using S1 and S2, and it is also the station with the least amount of data available (see Fig. 1). All of these results (except NIZN and SPIR stations) are consistent with Dai et al. (2002); Ortiz de Galisteo et al. (2011); Kalinnikov and Khutorova (2017).

For the coastal stations, the S1 amplitude is around 1 mm while S2 is around 0.3 mm. Moreover, as we travel from north to south on the coastal stations, the S1 peak hour propagates to earlier times from 8 UTC to 3 UTC while the S2 peak hour lags from S1 peak hour by 1–5 h and the explained variance of S2 increases from 3.2% to 31.8%. This behaviour ensures that the peak hour of the mean diurnal cycle for the coastal stations in JJA stays approximately at 6–7 UTC.

For the highland stations further east, the S1 amplitude is around 2 mm while S2 is around 0.6 mm. As opposed to the coastal stations' behaviour, as we move southwards on the highland stations, the S1 peak hour propagates to later times from 7 UTC to 13 UTC and the S2 peak hour lags from the S1 peak hour by 1–2 h while the explained variance of S2 stays around 7%.

For the Eastern stations, ELRO and KATZ stations behave in the same manner as the highland stations. By going south from SPIR station to ELAT station, the S1 amplitude increases while the S2 explained variance decreases from 53.1% to 9.8% with its amplitude fixed at 0.5–0.6 mm. The combined effect causes the peak hour in the mean diurnal cycle to propagate southwards from 16 UTC at SPIR station to 21 UTC at ELAT station. Finally, DSEA station has S1 and S2 amplitudes at 0.7 and 0.5 mm respectively with almost the same peak hour (4–5 UTC) and the explained variance is 62.1% for S1 and 33.3% for S2.

## 4. Discussion

Generally, the main transport mechanisms which drive PWV variability are large scale atmospheric changes such as high- and low-pressure systems (i.e., synoptic forcing) along with local winds with

**Table 3**
The diurnal and semidiurnal harmonic analysis parameters for the JJA months. A, P and V are the amplitude, peak hour and the explained variance respectively. VT is the total variance explained by S1 and S2.

| Station | Location | A1 [mm] | A2 [mm] | P1 [UTC] | P2 [UTC] | V1 [%] | V2 [%] | VT [%] |
|---|---|---|---|---|---|---|---|---|
| KABR | Coastal | 1.1 | 0.2 | 8 | 9 | 96.5 | 3.2 | 99.7 |
| BSHM | Coastal | 0.9 | 0.2 | 7 | 7 | 93.5 | 4.7 | 98.2 |
| CSAR | Coastal | 1.0 | 0.2 | 6 | 7 | 94.0 | 5.2 | 99.2 |
| TELA | Coastal | 0.8 | 0.2 | 5 | 6 | 90.4 | 8.4 | 98.7 |
| ALON | Coastal | 0.9 | 0.3 | 4 | 6 | 87.5 | 11.3 | 98.8 |
| SLOM[a] | Coastal | 0.7 | 0.5 | 3 | 8 | 63.6 | 31.8 | 95.3 |
| NIZN[a] | Coastal | 0.3 | 0.0 | 5 | 7 | 9.4 | 4.0 | 13.3 |
| NZRT | Highland | 1.5 | 0.4 | 7 | 9 | 93.0 | 6.6 | 99.5 |
| MRAV | Highland | 2.0 | 0.6 | 8 | 9 | 91.7 | 7.9 | 99.7 |
| YOSH | Highland | 2.0 | 0.6 | 10 | 11 | 91.1 | 8.4 | 99.5 |
| JSLM | Highland | 2.3 | 0.6 | 11 | 11 | 92.5 | 7.1 | 99.6 |
| KLHV | Highland | 1.7 | 0.5 | 10 | 11 | 91.7 | 7.2 | 98.9 |
| YRCM | Highland | 1.1 | 0.3 | 12 | 12 | 90.7 | 6.3 | 97.0 |
| RAMO | Highland | 1.4 | 0.3 | 13 | 1 | 96.0 | 3.5 | 99.5 |
| ELRO | Eastern | 1.7 | 0.6 | 11 | 10 | 89.5 | 10.1 | 99.6 |
| KATZ | Eastern | 1.6 | 0.6 | 9 | 10 | 88.2 | 11.4 | 99.6 |
| DRAG | Eastern | 2.5 | 0.3 | 10 | 1 | 97.7 | 1.7 | 99.5 |
| DSEA | Eastern | 0.7 | 0.5 | 4 | 5 | 62.1 | 33.3 | 95.4 |
| SPIR | Eastern | 0.4 | 0.5 | 0 | 4 | 20.4 | 53.1 | 73.5 |
| NRIF | Eastern | 1.0 | 0.5 | 20 | 6 | 76.5 | 22.5 | 98.9 |
| ELAT | Eastern | 1.8 | 0.6 | 0 | 7 | 89.5 | 9.8 | 99.3 |

[a] Station is located inland, see Fig. 1 for more accurate location.

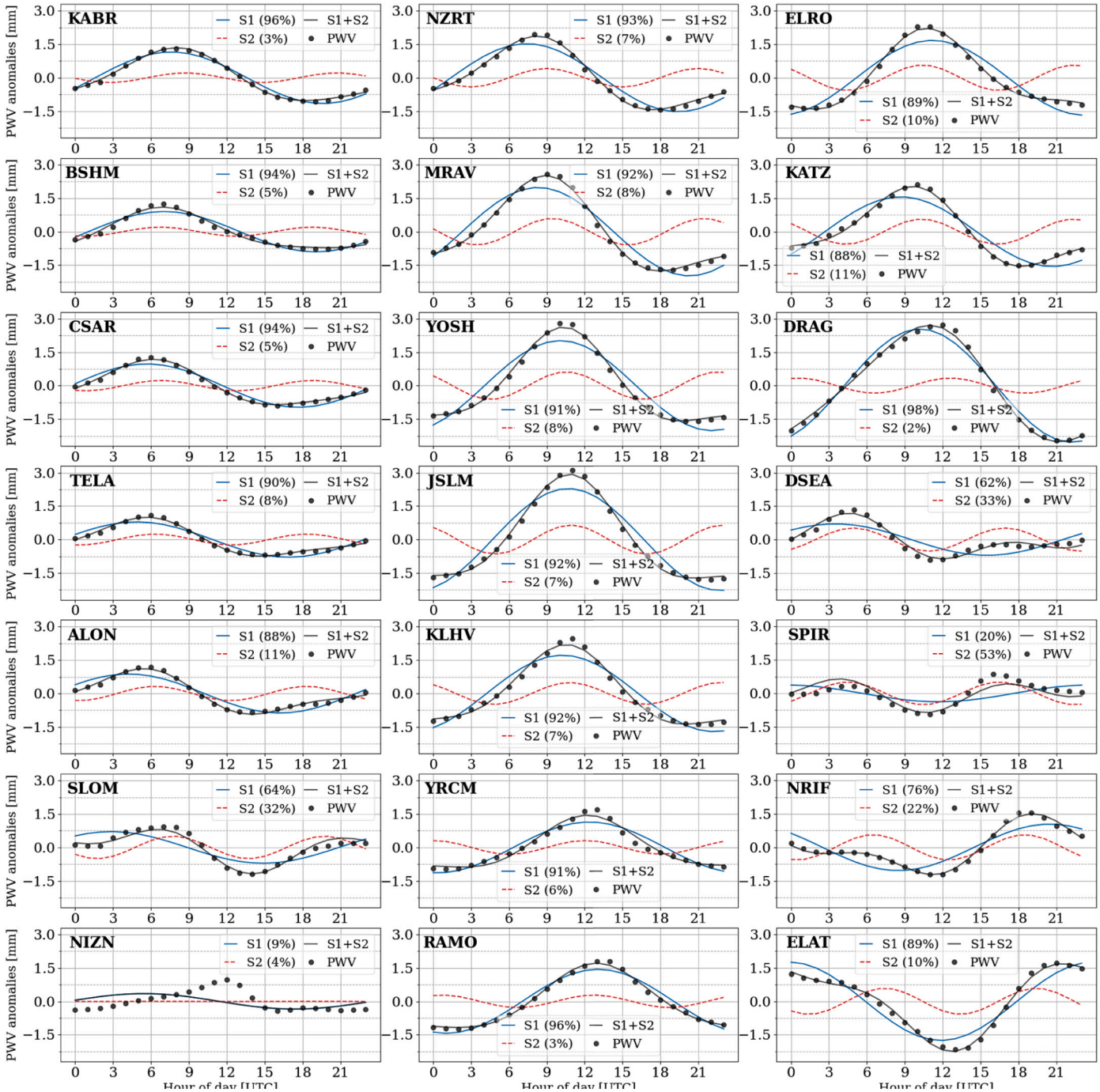


**Fig. 8.** The PWV diurnal and semidiurnal modes in JJA months (solid blue and red dashed), their sum (solid black) and the mean diurnal cycle in JJA months (black circles). The panel layout is the same as in Fig. 7. (For interpretation of the references to colour in this figure legend, the reader is referred to the web version of this article.)

varying degree of humidity (Kassomenos and McGregor, 2006; Wu et al., 2003). Since we average our PWV time series over a large number of days in order to remove any inter-daily synoptic forcing variations impacting on the PWV diurnal cycle, we expect to remain with the mean dominant synoptic situation for each season (Jakobson et al., 2009). However, for DJF, SON and MAM months the Eastern Mediterranean region typically experiences a mixture of different synoptic situations which create considerable variability in the daily humidity values. On the other hand, the summer in the Eastern Mediterranean (JJA months) has the most persistent and stable synoptic forcing associated with the Persian Troughs and their accompanying subtropical Highs (Alpert et al., 2004) than any other season. Consequently, we focus our discussion here on the PWV diurnal cycle in the summer JJA months.

### 4.1. PWV diurnal cycle in JJA months

The first major feature in Fig. 7 is that the PWV diurnal amplitude in JJA is the highest, followed by MAM, SON and DJF. A straightforward explanation can be derived from Clausisus-Clapeyron's equation, stating that warm air can hold more water vapor before condensing to form clouds of liquid droplets compared with an equivalent colder air parcel. However, we would expect the PWV to peak at approximately the same time as when the temperature peaks, at around 11–12 UTC. This is clearly not the case for the coastal stations which peak at 6–7 UTC. Nevertheless, the large diurnal temperature differential in JJA months allows for a stronger MSB cycle.

Secondly, for most stations, the peak which is reached during daytime is higher than the night-time minimum. This is consistent with the weak dry land breeze that needs to overcome the western Etesian winds due to the synoptic forcing. And, primarily, with the higher daily unstable mixed-layer boundary height as compared to lower and stable nocturnal boundary-layers (as discussed further below).

Third, for the highland stations, we notice a propagation of the PWV diurnal peak hour amplitude as we move from north to south. As the MSB travels inland it changes direction from a mean direction of west to west-north due to the Coriolis effect (Neumann, 1977; Alpert et al., 1984). Furthermore, Naor et al. (2017) studied the MSB penetration to the Jordan Valley Rift (JRF) and found that the distance to the Mediterranean Sea shore, among other topographical features, dictated the timing of the MSB arrival. Thus, Fig. 9 shows the PWV peak hour of each station in JJA months versus its distance to the Mediterranean Sea shore. Clearly, there is a linear trend, i.e., it takes time for the MSB to travel the distance from the coast and reach each station. Nevertheless, we must take care with this trend since after sunset (orange line) the MSB gradually weakens and stops while the linear trend continues. This suggests the existence of different humidity transport mechanism involved for the south-eastern stations as shown theoretically by Rotunno (1983). Moreover, for the Dead Sea (DSEA) station, the peak hour does not correlate with the distance to shore probably since it resides in a location with its own unique micro-climate as well as another local supply of humidity (Kunin et al., 2019).

The strongest features of Fig. 7 in JJA months are the relatively low amplitude and early peak hour of the coastal stations as opposed to the highland stations. The early peak is consistent with the MSB explanation since the see breeze front reaches the coastal stations at approximately the same time (Alpert and Rabinovich-Hadar, 2003). The low PWV amplitude for the coastal stations is consistent if we consider the Mixing Layer Hight (MLH) as a modulating factor for the PWV diurnal cycle. Uzan et al. (2016, 2019) demonstrated this fact by the use of ceilometers to measure the mixing layer height for two stations near the Israeli coast. Using the data measured from the same case-study, Fig. 10 shows the diurnal evolution of mixing layer height and PWV for the TELA and JSLM GNSS stations for two Augusts (in 2015 and 2016). We can see that the diurnal evolution of the mixing layer height correlates with the PWV, where in the Tel-Aviv (TELA) station we see that the mixing layer height is higher in the morning and lower in the evening and in the Jerusalem (JSLM) station the mixing layer height peaks roughly at noon where it overlaps the PWV peak. Moreover, the difference between maximum and minimum values in Tel-Aviv is approximately 2 mm while for Jerusalem it is around 6 mm giving a ratio of 1/3 which is consistent with Fig. 7. The mixing layer height max-min difference has roughly the same ratio as the PWV (200 m in TELA and 750 m in JSLM). Therefore, we suggest that the mixing layer height modulates the diurnal PWV, at least in summer over the Eastern Mediterranean. The low mixing layer height along the coast inhibits the effectiveness of the MSB to advect humidity hence the low PWV diurnal amplitude. The

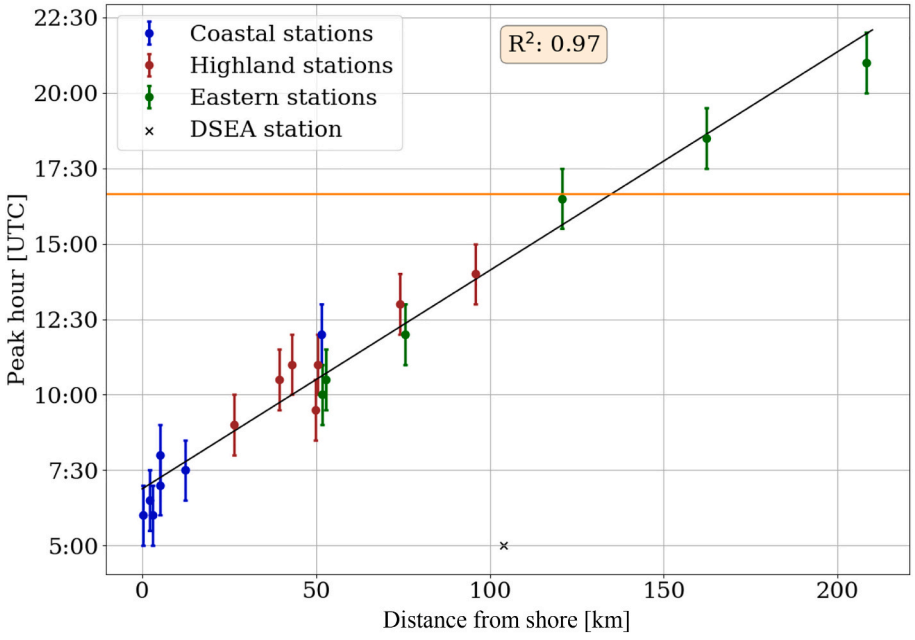


**Fig. 9.** The peak hour of the diurnal PWV cycle in JJA months for each station vs. the station's distance to the Mediterranean Sea shore. The error bars are of 1-h and represent the peak hour's uncertainty. The orange horizontal line represents the mean JJA months sunset time (UTC). (For interpretation of the references to colour in this figure legend, the reader is referred to the web version of this article.)

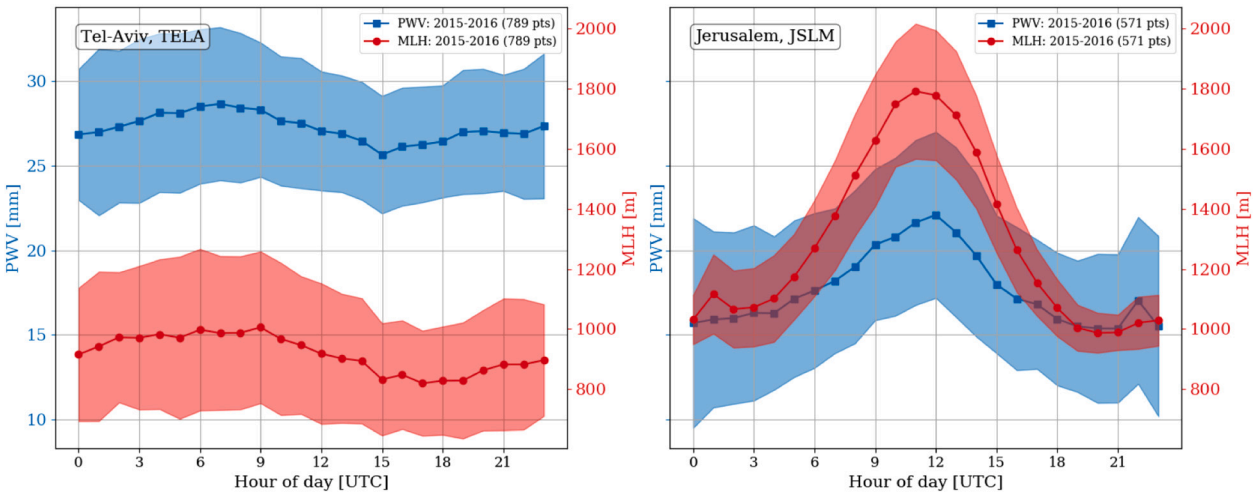


**Fig. 10.** A comparison between the GNSS-PWV diurnal mean cycles (blue squares) and Mixing Layer Height (MLH - from ceilometers, red circles) for the TELA (left) and JSLM (right) stations for Augusts 2015 and 2016. The filled area represents the STD for each set of measurements. (For interpretation of the references to colour in this figure legend, the reader is referred to the web version of this article.)

higher mixing layer height in the highlands however, allows the MSB to be more pronounced and subsequently increasing the PWV diurnal amplitude. This result suggests that a careful investigation of the correlation between the MLH and the PWV on a diurnal time scale is needed. For example, what is the sensitivity of this correlation to topography? how can we exploit this correlation if it is confirmed via other active sensing devices? (e.g., partition the PWV into two components). Another possible application of this connection is to is to suggest a potential correction to the diurnal MLH value on a global scale where PWV is readily available from multiple GNSS stations. However, this correlation needs to be first substantiated empirically by other active sensing devices.

Finally, evaporation and evapotranspiration can be considered as sources for the PWV diurnal cycle while condensation and precipitation are considered as sinks. Although precipitation during the summer months in the Eastern Mediterranean is rare to non-existent due to the stable synoptic forcing, nocturnal condensation of humidity and the subsequent evaporation in the morning (a few hours after sunrise) at the coastal stations does take place and should explain some of the PWV diurnal variability. However, separating these processes' contribution to the diurnal PWV from the MSB arriving approximately at the same time proves difficult.

### 4.2. Harmonic analysis in JJA months

Dai et al. (2002) employed an harmonic analysis on the PWV diurnal variations derived from 54 GPS stations in North America with a data period span of 1–2 years. They found out that it is sufficient to take into account only the first two modes (S1 and S2) since they explain more than 95% of the mean sub-daily variance in summer, where the diurnal mode is the dominant mode followed by the much weaker semidiurnal mode. These results are further substantiated by the work of Ortiz de Galisteo et al. (2011) who analysed the PWV diurnal harmonics derived from 10 GPS stations in Spain with a data period of 7 years and was able to explain more than 97% of the variance with the first two modes in summer. Finally, Kalinnikov and Khutorova (2017) analysed the PWV diurnal harmonics derived from 16 GPS stations in the Volga–Ural region of Russia with a data period of 2 years and showed that the first two harmonics explain more than 90% of the variance for all the stations in summer. With the addition of our results, the successful explanation of the mean diurnal PWV variations with the first two harmonic modes, at least in summer, implies physical processes that have the periods of 24 and 12 h. However, what physical process can we deduce from the semidiurnal mode existence? Cook (2012) suggested that the semidiurnal harmonic of the excess insolation accounts for the long wave cooling at night-time (Fig. 3 at Cook (2012)), thus any linear response driven by the diurnal insolation cycle contains similar harmonics. They demonstrated this behaviour with the mean diurnal temperature, wind and pressure cycles. Hence, we must conclude that this behaviour can be applied also to the diurnal PWV.

Looking at the middle column (highlands) in Fig. 8, we see that the second peak of the semidiurnal mode is from 21:00 to 00:00, thus somewhat offsetting the night-time departure from the diurnal mode. However, for the coastal stations, this offsetting occurs earlier, approximately 2–3 h after sunset. The amplitude of the semidiurnal mode increases southwards with the coastal stations and roughly decreases southwards with the highland stations. All this variability suggests a different nocturnal PWV response for each station that is likely to be dependant on the local topography, that dictates the wind regime (e.g., katabatic and anabatic winds).

We should emphasize that Jin et al. (2008) showed the existence of the diurnal and semidiurnal modes in tropospheric ZTD derived from GPS signals on a global scale. Their results were consistent with classical atmospheric tide theory (Chapman and Lindzen, 1970), mainly due to the hydrostatic component (ZHD) in the ZTD term which is highly sensible to atmospheric pressure. However, PWV is extracted by subtracting the ZHD from the ZTD thus eliminating the pressure dependency. Therefore, the role of atmospheric tides in the PWV spatio-temporal distribution remains uncertain and requires further investigation.

## 5. Conclusions

Our aim in this work is to produce and analyse the annual and seasonal mean diurnal PWV climatology in the Eastern Mediterranean region. To this end, we processed and analysed the 5-min averaged PWV time series using the ZWD derived from 21 SOI-APN of ground receivers with data periods of 5 to 21 years. The main findings of this work are as follows:

- The combination of GNSS ground receiver network's data and processing software such as GipsyX allows for a successful recovery of diurnal PWV variations and enables the production of the PWV diurnal climatology of the Eastern Mediterranean region. Furthermore, this tool can be utilized to explore the long-term PWV variations of this region.

- The diurnal amplitude in summer is the highest compared to the seasonal mean for most stations followed by spring and autumn, while the weakest diurnal amplitude is in winter. Generally, the diurnal amplitude in the highlands is higher than in the eastern stations followed by the coastal areas which have the weakest diurnal amplitude compared to the mean.
- In summer, for all the stations except the Dead Sea (DSEA), the peak hour of the diurnal cycle correlates with the distance of the station to the Mediterranean Sea shore, suggesting that the Mediterranean Sea Breeze (MSB) is a key driver of humidity on the diurnal time scale.
- The PWV diurnal cycle is correlated with the Mixing Layer Height (MLH) diurnal variations during summer, suggesting that the boundary layer height is modulating the PWV in this region, however, further research is needed to establish this finding.
- The summer PWV diurnal variations were subjected to harmonic analysis which revealed that the diurnal and semidiurnal modes (S1 and S2) explain ~95% of the sub-daily variance in 19 out of 21 of the stations inside our network. For most stations, the diurnal mode has the largest amplitude followed by the weaker semidiurnal mode. Finally, whether the PWV diurnal variations contain the signature of atmospheric tides is unclear and requires further investigation.

## Author contributions

All authors have made significant contributions to the manuscript. Shlomi Ziskin Ziv processed the GPS-ZWD along with temperature and MLH ceilometers data, designed and implemented all the data handling algorithms development, wrote the main manuscript text and prepared all the figures and tables in the manuscript; Yoav Yair, Pinhas Alpert and Leenes Uzan revised the manuscript; Yuval Reuveni conceived and designed part of the algorithm development, analysed the data and results and is the main author who developed and revised the manuscript.

## Declaration of Competing Interest

The authors declare that they have no known competing financial interests or personal relationships that could have appeared to influence the work reported in this paper.

## Acknowledgements

This work was founded by the Israeli Ministry of Science, Technology & Space grants 3-14517 and 3-15743. We would also like to acknowledge SOPAC data center (http://garner.ucsd.edu/) for letting us gain access to the RINEX files used in this work. We would also like to thank the Israeli Meteorological Service (https://ims.gov.il/en) for the temperature data from the automated stations and for the radiosonde data. Finally, we would like to thank Leenes Uzan for the final processed MLH data of Tel-Aviv and Jerusalem stations.

## Appendix A. Bet-Dagan radiosonde PWV validation

For the validation of the GNSS derived PWV with the radiosonde derived PWV, we chose the closest GNSS station (TELA) to Bet-Dagan radiosonde station (see the map at Fig. 1) and compared the two PWV time series. The Bet-Dagan radiosonde derived PWV is calculated using the following equation:

$$\mathrm{PWV} = \int (\rho \cdot Q) dz \tag{A1}$$

where $\rho$ and Q are the air density and specific humidity at height z respectively. Because of the low sampling rate of the data in Bet-Dagan (X2 daily) as opposed to the TELA GNSS station (5 min), one must choose how to address a comparison between the two stations. We chose to average the PWV from TELA station during the times of the radiosonde launch and the maximum possible height achieved by it. The mean time of the flight of the radiosonde is about an hour and a half, during which the PWV from TELA station does not change considerably (not shown).

Fig. A1 shows the comparison of the PWV of Bet-Dagan station and that of TELA GNSS station. While there is small bias, there is quite a skew in the residual distribution. To investigate this abnormality, we plotted Bet-Dagan's PWV time series ontop of the TELA PWV time series, as you can see in Fig. A2. We see that the residuals are seasonal in nature and after August 2013 are constrained between $\sim -5$ to 5 mm. What happened in August 2013? Luckily for us, we were given the original physical reports of the soundings and were able to determine that the main sounding equipment was changed exactly at this date. Alas, the seasonality of the residuals, tough constrained, still makes us believe that there are more calibration/systematic errors in the radiosonde retrievals to be discovered and addressed properly.

If we compare the PWV between Bet-Dagan and TELA station for the years after the sounding equipment was replaced (i.e., 2014–2019), as can be seen in Fig. A3, we get a drop in the RMSE, and the disappearance of the skew that plagued us earlier with a sleight increase in bias. It is clear from Fig. A2 that the positive residuals prior to August 2013 contributed to the small bias and the more realistic bias is probably should be taken after August 2013.

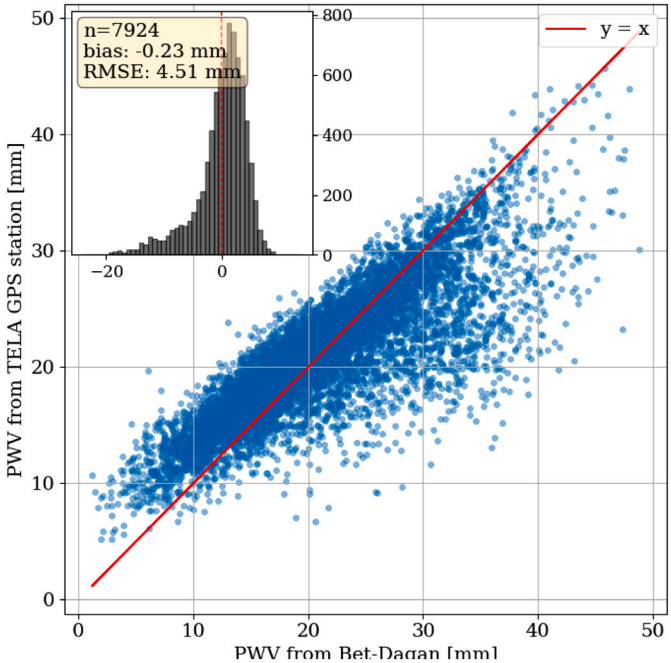


**Fig. A1.** A scatter plot of the PWV from TELA GNSS station vs. the PWV from Bet-dagan radiosonde station in 2007–2019. A 45-degree line is plotted (red) for comparison. Note the skew in the residual distribution with an RMSE of 4.37 mm and a small bias. (For interpretation of the references to colour in this figure legend, the reader is referred to the web version of this article.)

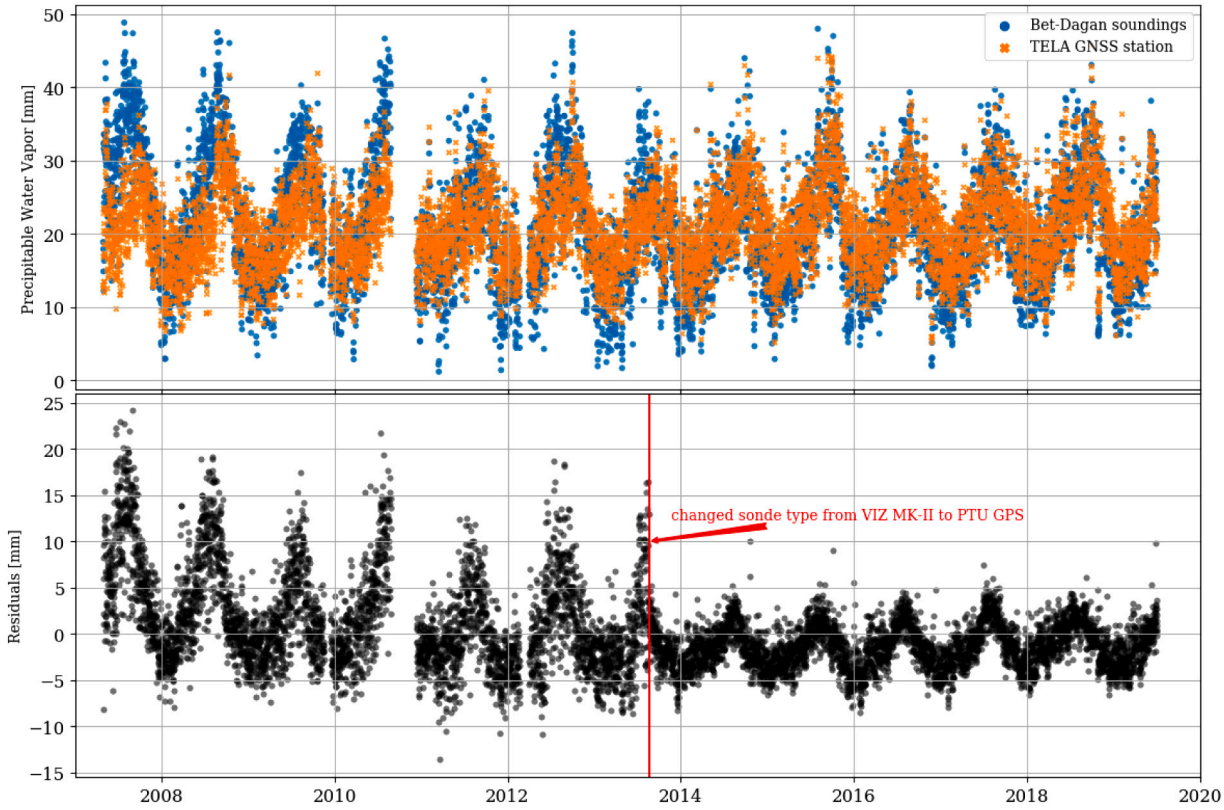


**Fig. A2.** Top: PWV from Bet-Dagan radiosonde station (blue circles) and from TELA GNSS station (orange x's) in 2007–2019. Bottom: residuals. Note the residuals become constrained from 08 to 2013 probably due to a radiosonde equipment change. (For interpretation of the references to colour in this figure legend, the reader is referred to the web version of this article.)

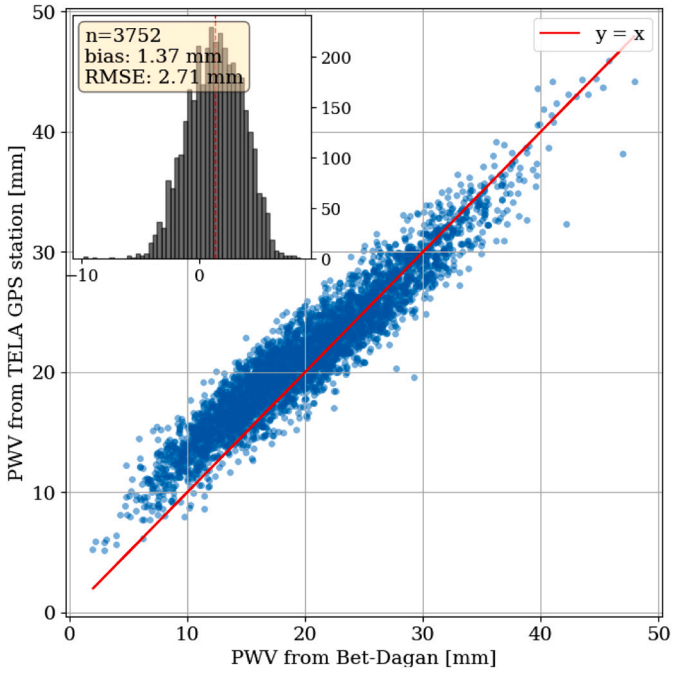


**Fig. A3.** A scatter plot of the PWV from TELA GNSS station vs. the PWV from Bet-Dagan radiosonde station in 2014–2019. A 45 degree line is plotted (red) for comparison. Note the relatively large bias and small RMSE. (For interpretation of the references to colour in this figure legend, the reader is referred to the web version of this article.)

## References


Alpert, P., Rabinovich-Hadar, M., 2003. Pre-and post-sea-breeze frontal lines—a Meso-γ-scale analysis over South Israel. J. Atmos. Sci. 60, 2994–3008.

Alpert, P., Kusuda, M., Abe, N., 1984. Anticlockwise rotation, eccentricity and tilt angle of the wind hodograph. Part II: an observational study. J. Atmos. Sci. 41, 3568–3583.

Alpert, P., Osetinsky, I., Ziv, B., Shafir, H., 2004. A new seasons definition based on classified daily synoptic systems: an example for the eastern Mediterranean. Int. J. Climatol. J. R. Meteorol. Soc. 24, 1013–1021.

Bar-Sever, Y.E., 2016. Real-Time GNSS Positioning with JPL's new GIPSYx Software. AGUFM 2016, G44A-04.

Bevis, M., Businger, S., Herring, T.A., Rocken, C., Anthes, R.A., Ware, R.H., 1992. GPS meteorology: remote sensing of atmospheric water vapor using the global positioning system. J. Geophys. Res.-Atmos. 97, 15787–15801.

Bevis, M., Businger, S., Chiswell, S., Herring, T.A., Anthes, R.A., Rocken, C., Ware, R.H., 1994. GPS meteorology: mapping zenith wet delays onto precipitable water. J. Appl. Meteorol. 33, 379–386.

Böhm, J., Niell, A., Tregoning, P., Schuh, H., 2006a. Global Mapping Function (GMF): a new empirical mapping function based on numerical weather model data. Geophys. Res. Lett. 33.

Böhm, J., Niell, A., Tregoning, P., Schuh, H., 2006b. Global Mapping Function (GMF): a new empirical mapping function based on numerical weather model data. Geophys. Res. Lett. 33.

Chapman, S., Lindzen, R., 1970. Atmospheric Tides. D. Reidel, Norwell, Mass, p. 200.

Chen, B., Liu, Z., 2016. Global water vapor variability and trend from the latest 36 year (1979 to 2014) data of ECMWF and NCEP reanalyses, radiosonde, GPS, and microwave satellite. J. Geophys. Res.-Atmos. 121, 11–442.

Cook, N.J., 2012. The atmospheric tide and the sea–land breeze cycle in Jersey. Weather 67, 184–187.

Cressie, N., 1988. Spatial prediction and ordinary kriging. Math. Geol. 20, 405–421.

Crosman, E.T., Horel, J.D., 2010. Sea and lake breezes: a review of numerical studies. Bound.-Layer Meteorol. 137, 1–29.

Dai, A., Wang, J., Ware, R.H., Van Hove, T., 2002. Diurnal variation in water vapor over north america and its implications for sampling errors in radiosonde humidity. J. Geophys. Res.-Atmos. 107, ACL-11.

Davis, J., Herring, T., Shapiro, I., Rogers, A., Elgered, G., 1985. Geodesy by radio interferometry: effects of atmospheric modeling errors on estimates of baseline length. Radio Sci. 20, 1593–1607.

Dayan, U., Lifshitz-Goldreich, B., Pick, K., 2002. Spatial and structural variation of the atmospheric boundary layer during summer in Israel—Profiler and Rawinsonde measurements. J. Appl. Meteorol. 41, 447–457.

Duan, J., Bevis, M., Fang, P., Bock, Y., Chiswell, S., Businger, S., Rocken, C., Solheim, F., van Hove, T., Ware, R., et al., 1996. GPS meteorology: direct estimation of the absolute value of precipitable water. J. Appl. Meteorol. 35, 830–838.

Elliott, W., Smith, M., Angell, J., 1991. Monitoring tropospheric water vapor changes using radiosonde data. In: Developments in Atmospheric Science, 19. Elsevier, pp. 311–327.

Eueler, H.-J., Goad, C.C., 1991. On optimal filtering of GPS dual frequency observations without using orbit information. Bull. Géodésique 65, 130–143.

Ichoku, C., Levy, R., Kaufman, Y.J., Remer, L.A., Li, R.-R., Martins, V.J., Holben, B.N., Abuhassan, N., Slutsker, I., Eck, T.F., et al., 2002. Analysis of the performance characteristics of the five-channel microtops II sun photometer for measuring aerosol optical thickness and precipitable water vapor. J. Geophys. Res.-Atmos. 107, AAC-5.

Jakobson, E., Ohvril, H., Elgered, G., 2009. Diurnal Variability of Precipitable Water in the Baltic Region, Impact on Transmittance of the Direct Solar Radiation.

Jin, S., Wu, Y., Heinkelmann, R., Park, J., 2008. Diurnal and semidiurnal atmospheric tides observed by co-located GPS and VLBI measurements. J. Atmos. Sol. Terr. Phys. 70, 1366–1372.

Kalinnikov, V.V., Khutorova, O.G., 2017. Diurnal variations in integrated water vapor derived from a GPS ground network in the Volga-Ural region of Russia. Ann. Geophys. 09927689, 35.

Kassomenos, P., McGregor, G., 2006. The interannual variability and trend of precipitable water over southern Greece. J. Hydrometeorol. 7, 271–284.

Kunin, P., Alpert, P., Rostkier-Edelstein, D., 2019. Investigation of sea-breeze/foehn in the Dead Sea valley employing high resolution WRF and observations. Atmos. Res. 229, 240–254.

Leontiev, A., Reuveni, Y., 2017. Combining Meteosat-10 satellite image data with GPS tropospheric path delays to estimate regional integrated water vapor (IWV) distribution. Atmosph. Meas. Tech. 10, 537.

Leontiev, A., Reuveni, Y., 2018. Augmenting GPS IWV estimations using spatio-temporal cloud distribution extracted from satellite data. Sci. Rep. 8, 1–10.

Li, Z., Muller, J.-P., Cross, P., 2003. Comparison of precipitable water vapor derived from radiosonde, GPS, and Moderate-Resolution Imaging Spectroradiometer measurements. J. Geophys. Res.-Atmos. 108.

Miloshevich, L.M., Vömel, H., Whiteman, D.N., Lesht, B.M., Schmidlin, F., Russo, F., 2006. Absolute accuracy of water vapor measurements from six operational radiosonde types launched during AWEX-G and implications for AIRS validation. J. Geophys. Res.-Atmos. 111.

Naor, R., Potchter, O., Shafir, H., Alpert, P., 2017. An observational study of the summer Mediterranean Sea breeze front penetration into the complex topography of the Jordan Rift Valley. Theor. Appl. Climatol. 127, 275–284.

Neumann, J., 1977. On the rotation rate of the direction of sea and land breezes. J. Atmos. Sci. 34, 1913–1917.

Ortiz de Galisteo, J.P., Cachorro, V., Toledano, C., Torres, B., Laulainen, N., Bennouna, Y., De Frutos, A., 2011. Diurnal cycle of precipitable water vapor over Spain. Q. J. R. Meteorol. Soc. 137, 948–958.

Pérez-Ramírez, D., Whiteman, D.N., Smirnov, A., Lyamani, H., Holben, B.N., Pinker, R., Andrade, M., Alados-Arboledas, L., 2014. Evaluation of AERONET precipitable water vapor versus microwave radiometry, GPS, and radiosondes at ARM sites. J. Geophys. Res.-Atmos. 119, 9596–9613.

Reuveni, Y., Kedar, S., Owen, S.E., Moore, A.W., Webb, F.H., 2012. Improving sub-daily strain estimates using GPS measurements. Geophys. Res. Lett. 39.
Reuveni, Y., Kedar, S., Moore, A., Webb, F., 2014. Analyzing slip events along the Cascadia margin using an improved subdaily GPS analysis strategy. Geophys. J. Int. 198, 1269–1278.
Reuveni, Y., Bock, Y., Tong, X., Moore, A.W., 2015. Calibrating interferometric synthetic aperture radar (InSAR) images with regional GPS network atmosphere models. Geophys. J. Int. 202, 2106–2119.
Rodwell, M.J., Hoskins, B.J., 1996. Monsoons and the dynamics of deserts. Q. J. R. Meteorol. Soc. 122, 1385–1404.
Rotunno, R., 1983. On the linear theory of the land and sea breeze. J. Atmos. Sci. 40, 1999–2009.
Ryu, Y.-H., Smith, J.A., Bou-Zeid, E., 2015. On the climatology of precipitable water and water vapor flux in the mid-Atlantic region of the United States. J. Hydrometeorol. 16, 70–87.
Shilo, E., Ziv, B., Shamir, E., Rimmer, A., 2015. Evaporation from Lake Kinneret, Israel, during hot summer days. J. Hydrol. 528, 264–275.
Simpson, J.E., 1994. Sea Breeze and Local Winds. Cambridge University Press.
Soden, B.J., Turner, D.D., Lesht, B.M., Miloshevich, L.M., 2004. An analysis of satellite, radiosonde, and lidar observations of upper tropospheric water vapor from the Atmospheric Radiation Measurement Program. J. Geophys. Res.-Atmos. 109.
Thayer, G.D., 1974. An improved equation for the radio refractive index of air. Radio Sci. 9, 803–807.
Trenberth, K.E., Fasullo, J., Smith, L., 2005. Trends and variability in column-integrated atmospheric water vapor. Clim. Dyn. 24, 741–758.
Uzan, L., Egert, S., Alpert, P., 2016. Ceilometer evaluation of the eastern Mediterranean summer boundary layer height-first study of two Israeli sites. Atmosph. Meas. Tech. 9.
Uzan, L., Egert, S., Khain, P., Levi, Y., Vladislavsky, E., Alpert, P., 2019. Ceilometers as planetary boundary layer detectors and a corrective tool for ECMWF and COSMO NWP models. Atmosph. Chem. Phys. Discuss. 1–26.
Van Baelen, J., Aubagnac, J.-P., Dabas, A., 2005. Comparison of near–real time estimates of integrated water vapor derived with GPS, radiosondes, and microwave radiometer. J. Atmos. Ocean. Technol. 22, 201–210.
Van de Berg, L., Schmetz, J., Whitlock, J., 1995. On the calibration of the meteosat water vapor channel. J. Geophys. Res.-Atmos. 100, 21069–21076.
Velden, C.S., Hayden, C.M., Nieman, S.J.W., Paul Menzel, W., Wanzong, S., Goerss, J.S., 1997. Upper-tropospheric winds derived from geostationary satellite water vapor observations. Bull. Am. Meteorol. Soc. 78, 173–196.
Wang, J., Zhang, L., Dai, A., Van Hove, T., Van Baelen, J., 2007. A near-global, 2-hourly data set of atmospheric precipitable water from ground-based GPS measurements. J. Geophys. Res.-Atmos. 112.
Wang, Y., Yang, K., Pan, Z., Qin, J., Chen, D., Lin, C., Chen, Y., Lazhu Tang, W., Han, M., et al., 2017. Evaluation of precipitable water vapor from four satellite products and four reanalysis datasets against GPS measurements on the Southern Tibetan Plateau. J. Clim. 30, 5699–5713.
Webb, F., Zumberge, J., 1993. An Introduction to GIPSY/OASIS-II. JPL Publication D-11088. Jet Propulsion Laboratory, Pasadena, California.
Westwater, E.R., 1978. The accuracy of water vapor and cloud liquid determination by dual-frequency ground-based microwave radiometry. Radio Sci. 13, 677–685.
Wu, P., Hamada, J.-I., Mori, S., Tauhid, Y.I., Yamanaka, M.D., Kimura, F., 2003. Diurnal variation of precipitable water over a mountainous area of Sumatra Island. J. Appl. Meteorol. 42, 1107–1115.
Ziv, B., Saaroni, H., 2011. The contribution of moisture to heat stress in a period of global warming: the case of the Mediterranean. Clim. Chang. 104, 305–315.
Ziv, B., Saaroni, H., Alpert, P., 2004. The factors governing the summer regime of the eastern Mediterranean. Int. J. Climatol. J. R. Meteorol. Soc. 24, 1859–1871.